AIAA JOURNAL
Vol. 32, No. 1, January 1994

Quasi-One-Dimensional Modeling of a Free-Piston Shock Tunnel

P. A. Jacobs*
University of Queensland, St. Lucia, Queensland 4072, Australia

A Lagrangian formulation for the quasi-one-dimensional modeling of free-piston-driven shock tunnels is described. Three simulations of particular conditions for the T4 shock tunnel are then presented and compared with experimental measurements. The simulations provide very good estimates for both the shock speed and the nozzle-supply pressure obtained after shock reflection and also provide detailed information on the gasdynamic processes over the full length of the facility. This detailed information may be used to identify some of the causes for observed variations in nozzle-supply pressure.

Nomenclature

A = duct or tube area, m^2
a = speed of sound, m/s
C_v = specific heat at constant volume, J/kg/K
D = (effective) duct or tube diameter, m
E = total energy per unit mass $e + 1/2u^2$, J/kg
e = specific internal energy, J/kg
F_{loss} = effective force due to pipe-fitting losses, N
F_p = piston friction force, N
F_{wall} = wall shear force due to viscous effects, N
f = Darcy-Weisbach friction factor
H = total enthalpy, J/kg
h = heat transfer coefficient, J/s/m^2/K
j = cell index
K = viscous loss coefficient
L = length, m
M = Mach number
m = mass, kg
P = pressure, Pa
Pr = Prandtl number
q = heat transfer rate, J/s
R = gas constant, J/kg/K
Re = Reynolds number
r = duct or tube radius, m
St = Stanton number
T = temperature, K
t = time, s
U = state vector in the gasdynamics equations
$\bar{U}_L, \bar{U}_R$ = Riemann invariants
u = local velocity, m/s
V = piston velocity, m/s
x = position, m
γ = ratio of specific heats
$\Delta\pm$ = intermediate variable for interpolation
Λ = compressibility factor
λ = compression ratio
μ = viscosity, kg/m/s; friction coefficient
π = 3.14159...
τ = wall shear stress, Pa
Ω = recovery factor

Subscripts
aw = adiabatic wall condition
B = back of piston
exit = nozzle exit plane
F = front of piston
f = friction value
j = Lagrangian cell index
$j \pm 1/2$ = interface indices
L, R = left and right states for the Riemann solver
loss = pipe-fitting value
p = piston
s = nozzle supply (stagnation) condition
wall = wall condition

Superscript
$*$ = interface condition/Eckert reference condition/nozzle throat

Introduction

WITH the recent installation of free-piston shock tunnels[1,2] and the reactivation of older pulse facilities,[3,4] there has been renewed interest in the quasi-one-dimensional modeling of transient-flow facilities.[5–9] Reasons for this interest include 1) the need for more detailed information on the test-flow conditions, 2) the identification of secondary effects which affect the flow quality, 3) the identification and assessment of new operating conditions without risk to facility hardware, and 4) the validation of new design concepts.

This paper will consider the modeling and simulation of a particular facility, namely the T4 free-piston tunnel located at the University of Queensland. It will be demonstrated that dynamic modeling, based on quasi-one-dimensional gasdynamics, point-mass dynamics for the moving piston, and engineering correlations for wall-shear stress and heat transfer, provides a reasonably good simulation tool. This tool may then be used to provide data on some of the points mentioned earlier.

The T4 facility[10] is shown schematically in Fig. 1. It is essentially a reflected-shock tunnel driven by a free-piston compressor. The attraction of the free-piston compressor is that it can conveniently provide a range of driver gases at very high temperatures and pressures.

The compression tube initially contains helium (or mixed helium-argon) driver gas at approximately atmospheric pressure. A primary diaphragm, typically consisting of two sheets of mild steel, separates the compression tube from the shock tube. The shock tube initially contains the test gas and is separated from an evacuated nozzle and test section by a thin plastic diaphragm.

The operation of the facility is initiated by the release of the piston and its acceleration along the compression tube. The driving force is provided by a reservoir of compressed air (not shown in Fig. 1). The driver gas, between the piston and the primary diaphragm, is compressed until the rupture pressure of the diaphragm is exceeded. The ratio of initial driver gas volume to the driver gas volume just before rupture is the compression ratio λ.

After the diaphragm ruptures, the driver gas expands into the shock tube and shock compresses the test gas before it. The primary shock wave (or incident shock wave) travels the length of the

---

Received Dec. 16, 1992; presented as Paper 93-0352 at the AIAA 31st Aerospace Sciences Meeting, Reno, NV, Jan. 11–14, 1993; revision received May 23, 1993; accepted for publication May 23, 1993.

*Research Fellow, Department of Mechanical Engineering. Member AIAA.

shock tube, reflects from the (nearly) closed end of the tube, and brings the test gas to rest in the "nozzle-supply region." Depending on the selected operating condition, temperatures and pressures in this region may reach typical values of 8000 K and 100 MPa, respectively.

Upon shock reflection, the light secondary diaphragm (located at the nozzle throat) ruptures, and test gas expands from nearly stagnant conditions in the nozzle-supply region to "steady" hypersonic flow conditions in the test section. The duration of this steady hypersonic flow is typically in the range of 0.5–2 ms. For the facility simulations presented here, the focus is on the performance of the free-piston compressor and shock tube only. Hence, the model will include the flow processes up to the nozzle throat but will ignore the nozzle starting process.

Numerical Modeling

The general procedure for modeling T4 is to divide the facility into its component parts such as the tubes, piston, diaphragms, and volumes of gas (i.e., gas slugs). The description of each component is formulated separately, and components are allowed to interact through boundary conditions. The core of the simulation is a time-stepping loop that first applies the specified boundary conditions and then advances the state of the entire system forward in time by a small increment (or time step). The generic components described in the following sections include a slug of compressible gas, a piston, and a diaphragm.

Facility Specification

In this one-dimensional formulation, the facility is modeled as a linear array of circular pipes aligned with the x axis. These pipes are, in increasing x distance, the compressed-air reservoir, the manifold with effective internal diameter $D = 0.168$ m, the compression tube, and the shock tube. See Table 1 for the component dimensions. At the downstream end of the shock tube, the nozzle is modeled by a contraction to $D^* = 0.025$ m and an expansion to $D_{\text{exit}} = 0.262$ m. All area variations are gradual and occur over distances of 0.1–0.2 m. This is in contrast to the sudden area transitions found in the actual facility. Referring to Fig. 1, the junction between the manifold and the compression tube is located at $x = 0$, whereas the primary diaphragm is located at $x = 26.0$ m (the compression-tube/shock-tube junction), and the light secondary diaphragm is located at $x = 36.0$ m. Shock-speed measuring stations 1, 2, and 3 are located at $x = 30.0$, 32.0, and 34.0 m, respectively.

Four gas slugs are modeled. These are 1) the slug of compressed-air pusher gas upstream of the piston, 2) the driver gas, initially between the piston and the main diaphragm, 3) the test gas, initially retained between the two diaphragms, and 4) a slug of very low pressure gas downstream of the secondary diaphragm. The simulations presented here will include both pure helium and a helium-argon mixture for the driver gas. Air will be the only test gas considered. Both the compressed air and the driver gas are modeled as perfect gases, whereas the test gas and the very low pressure gas initially in the nozzle are assumed to be in chemical equilibrium.

The piston is modeled as a rigid body. The initial position of its centroid is $x = 0.235$ m, and a buffer is included at the end of the compression tube so that the centroid position is limited to $x <= 25.765$ m.

Gasdynamics

Each slug of gas is divided into a number of control-mass elements (or cells) moving in a variable-area duct. Flow in one dimension only is considered, and any area changes in the tube area are assumed to be gradual. Although the boundary layer along the tube wall is not completely modeled in the formulation of the gasdynamic equations, some of its effects are modeled by the addition of a wall shear stress in the momentum equation and heat transfer in the energy equation.

Figure 2 shows a typical control-mass cell (labeled j) with interfaces (labeled $j - 1/2$ and $j + 1/2$) to adjacent cells. At each inter-

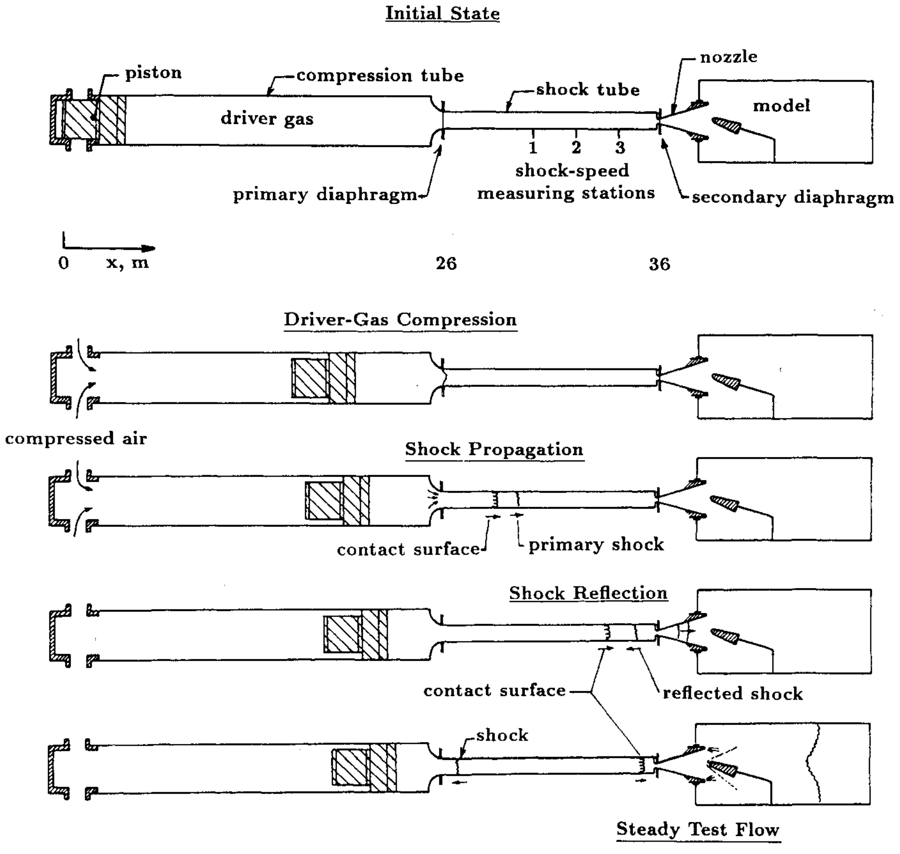

Fig. 1 Schema of the T4 shock tunnel facility and its operation.

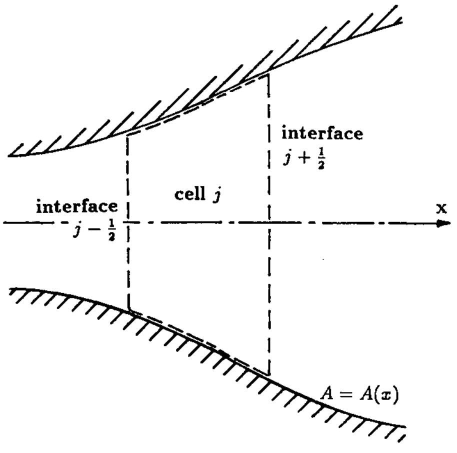

Fig. 2 Control-mass cell.

Table 1 T4 shock tunnel dimensions used in the simulations

Component	Diameter, m	Length, m	Mass, kg
Compressed-air reservoir	0.173	11.3	——
Manifold	0.168	1.0	——
Compression tube	0.229	26.0	——
Sock tube	0.076	10.0	——
Piston	0.229	0.47	92.0

face, the Lagrangian description equates the local fluid velocity to the interface velocity as

$$\frac{\mathrm{d}x_{j\pm 1/2}}{\mathrm{d}t} = u_{j\pm 1/2} \tag{1}$$

where u is computed with a Riemann solver. See Ref. 11 for an early application of the Lagrangian formulation.

The average density within the cell is given by

$$\bar{\rho}_j = \frac{m_j}{\bar{A}_j\,(x_{j+1/2} - x_{j-1/2})} \tag{2}$$

where barred quantities represent cell averages.

The rate of change of momentum in the cell is due to the pressure forces acting on the cell interfaces and viscous forces acting at the duct wall. It is given by

$$\begin{aligned}\frac{\mathrm{d}}{\mathrm{d}t}m_j\bar{u}_j = {} & [P_{j-1/2}A_{j-1/2} - P_{j+1/2}A_{j+1/2} \\ & + \bar{P}_j\,(A_{j+1/2} - A_{j-1/2}) - \overline{F_{\text{wall}}} - \overline{F_{\text{loss}}}\,]\end{aligned} \tag{3}$$

The rate of change of energy within the cell is due to the work done at the cell interfaces plus the heat transferred through the duct wall. It is given by

$$\frac{\mathrm{d}}{\mathrm{d}t}m_j\bar{E}_j = [P_{j-1/2}A_{j-1/2}u_{j-1/2} - P_{j+1/2}A_{j+1/2}u_{j+1/2} + \bar{q}_j] \tag{4}$$

The governing differential equations for the gasdynamics [(i.e., Eqs. (1), (3), and (4)] are completed by specifying the thermodynamic properties of the gas. For a perfect driver gas, the equation of state is

$$P = \rho RT \tag{5}$$

and, if the gas is considered to be calorically perfect, the specific internal energy is

$$e = C_v T \tag{6}$$

The equation of state may then be written as

$$P = \rho(\gamma - 1)e \tag{7}$$

and the speed of sound is given by

$$a^2 = \gamma RT = \gamma\frac{P}{\rho}P\rho = \gamma(\gamma - 1)e \tag{8}$$

For the air test gas, which is assumed to be in chemical equilibrium, the curve fits given in Ref. 12 are used to obtain P, T, a, and γ as functions of ρ and e for temperatures up to 25,000 K.

The viscous shear force on a gas cell is given by

$$\overline{F_{\text{wall}}} = \tau_{\text{wall}}\pi\bar{D}\,(x_{j+1/2} - x_{j-1/2}) \tag{9}$$

Assuming a circular cross section

$$\bar{D} = 2\,(\bar{A}/\pi)^{1/2} \tag{10}$$

The wall shear stress is obtained from the Darcy formula for steady incompressible flow (see, for example, Ref. 13)

$$\tau_{\text{wall}} = \frac{-\rho f u|u|}{8} \tag{11}$$

The friction factor is computed as[6]

$$\begin{aligned} f &= \frac{64}{\Lambda Re}, \quad Re < 2.0\times 10^3 \\ f &= \frac{0.032}{\Lambda}\left[\frac{Re}{2000}\right]^{0.3187}, \quad 2.0\times 10^3 \le Re \le 4.0\times 10^3 \\ f &= \frac{1}{\Lambda}\,[1.8\,\log_{10}(Re) - 1.5147]^{-2}, \quad Re > 4.0\times 10^3 \end{aligned} \tag{12}$$

where the Re is based on tube diameter

$$Re = \frac{\rho^* D|u|}{\mu^*} \tag{13}$$

Note that, for the turbulent regime, a smooth wall is assumed. The properties μ^* and $\rho^* = \rho T/T^*$ are evaluated at the Eckert reference temperature (see, for example, Ref. 14, Sec. 5.12),

$$T^* = T + 0.5(T_{\text{wall}} - T) + 0.22\,(T_{aw} - T) \tag{14}$$

where T is the cell-average temperature, T_{wall} is the specified wall temperature, and

$$T_{aw} = \Lambda T \tag{15}$$

is the adiabatic wall temperature. A compressibility correction is applied via the factor[15]

$$\Lambda = 1 + \frac{(\gamma - 1)}{2}\,\Omega M^2 \tag{16}$$

For laminar flow (i.e., $Re < 2.0 \times 10^3$), the recovery factor is set to $\Omega = (Pr)^{1/2}$, whereas for turbulent flow, $\Omega = (Pr)^{1/3}$.

Pressure losses due to sudden changes in tube cross section are computed for each cell as

$$\overline{F_{\text{loss}}} = \frac{\Delta P_{\text{loss}}}{L_{\text{loss}}} \bar{A}\,(x_{j+1/2} - x_{j-1/2}) \tag{17}$$

where

$$\Delta P_{\text{loss}} = -K_L 1/2 \rho u |u| \tag{18}$$

and L_{loss} is the length of tube over which the pressure loss is distributed. Values of K_L/L_{loss} are stored along with the cross-sectional area for the tube. For a contraction and a diaphragm station, $K_L = 0.25$ is used.

Heat transfer into a gas cell is given by (Ref. 14, Sec. 5.12)

$$q = h \pi \bar{D}\,(x_{j+1/2} - x_{j-1/2})(T_w - T_{aw}) \tag{19}$$

where the heat transfer coefficient is

$$h = \rho C_p |u| St \tag{20}$$

and the Stanton number is given by the modified Reynolds analogy for turbulent flow in pipes (see, for example, Ref. 14, Sec. 6.2)

$$St = \frac{f}{8} Pr^{-2/3} \tag{21}$$

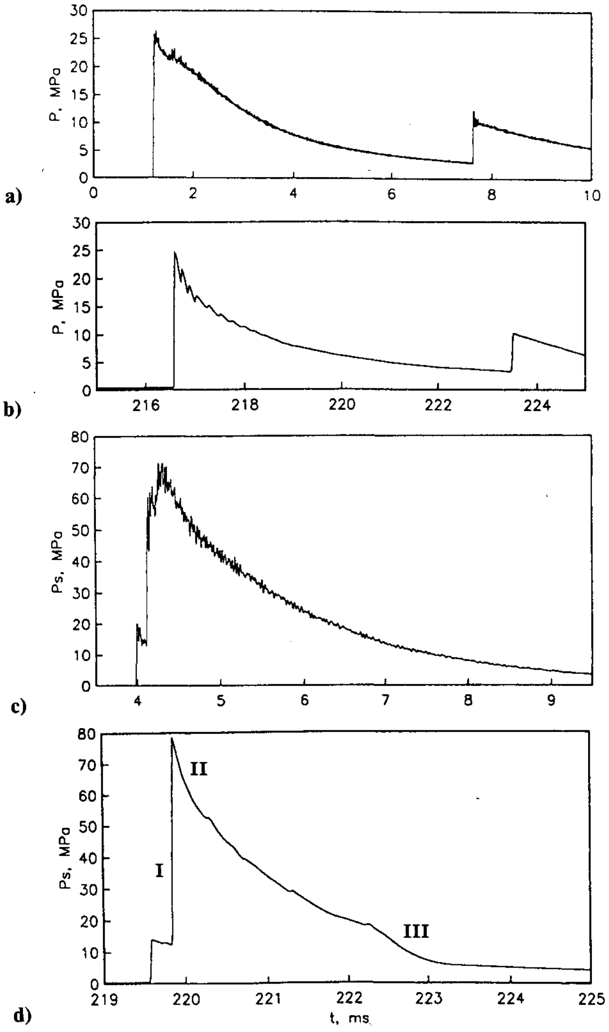

Fig. 3 Pressure histories for shot 1098: a) measured pressure at shock station 1; b) computed pressure at shock station 1; c) measured pressure in the nozzle-supply region; and d) computed pressure in the nozzle-supply region.

The dynamic viscosity of the gas is given by the Sutherland expression

$$\mu = \mu_0 \left(\frac{T}{T_0}\right)^{3/2} \left(\frac{T_0 + S_1}{T + S_1}\right) \tag{22}$$

where values of μ_0, T_0, and S_1 are set for each type of gas. The viscosities for mixtures of gases are obtained from Wilke's[16] expression. Following Ref. 6, the Prandtl number is given approximately as

$$Pr = \frac{20\gamma}{39\gamma - 15} \tag{23}$$

The pressures and velocities used in Eqs. (3) and (4) are obtained by first interpolating the flow state (consisting of a set of values for ρ, u, v, e, P, and a) from the cell centers to either side of each interface at the start of the time step and then applying the Riemann solver described in Ref. 17 to estimate the flow states at the interfaces during the time step. Note that this Riemann solver does not consider area variations or chemical reactions as do the generalized solvers in Refs. 18 and 19. However, Lappas et al.[20] indicate that, in their study, a simple solver for the self-similar Riemann problem gave simulation results that were just as good as results produced by the generalized solver in Ref. 18.

The state of the flow on either side of each interface L and R is interpolated (or reconstructed) from the set of cell-averaged states by assuming a linear variation of the variables within cells. This interpolation is performed separately for each primary variable. For example, the density on either side of the interface $(j + 1/2)$ is obtained by a nonlinear interpolation (or reconstruction) using the expressions

$$\begin{aligned} \rho_L &= \rho_j + (x_{j+1/2} - x_j)\,\text{minmod}\,[(\Delta -)_j, (\Delta +)_j] \\ \rho_R &= \rho_{j+1} + (x_{j+1/2} - x_{j+1})\,\text{minmod}\,[(\Delta -)_{j+1}, (\Delta +)_{j+1}] \end{aligned} \tag{24}$$

where

$$\begin{aligned} (\Delta -)_j &= \frac{\rho_j - \rho_{j-1}}{x_j - x_{j-1}} \\ (\Delta +)_j &= \frac{\rho_{j+1} - \rho_j}{x_{j+1} - x_j} \end{aligned} \tag{25}$$

represent two possible estimates of the slope of the density for cell j, and x_{j-1}, x_j, and x_{j+1} are the midpoints of the cells $j - 1$, j, and $j + 1$, respectively. The minmod limiter function selects the slope with the minimum magnitude if both slopes have the same sign and returns to zero otherwise (see, for example, Ref. 21).

Before interpolation, the inviscid boundary conditions are applied by setting up two layers of ghost cells at each of the boundaries. For a supersonic inflow boundary, all of the ghost cell quantities are specified as fixed. For a supersonic outflow boundary, the ghost-cell quantities are extrapolated from active cells just inside the boundary. Solid-wall (i.e., reflective) boundary conditions are applied by setting all of the scalar quantities in the ghost cells equal to those in the active cells adjacent to the boundary but setting the ghost cell velocities to the negative of the velocities in the active cells. Where two gas slugs interact, data between the two end cells of the first slug and the corresponding ghost cells of the second slug are exchanged.

Where the gas interacts with a piston (or endwall), the boundary-interface velocity u^* is specified. The interface pressure P^* may then be determined from the isentropic relations that, for a right-end boundary, give

$$P^* = \left[(\bar{U}_L - u^*) \frac{(\gamma - 1)}{2\gamma^{1/2}} \left(\frac{\rho_L}{P_L^{1/\gamma}} \right)^{1/2} \right]^{2\gamma/(\gamma - 1)} \tag{26}$$

Similarly, the interface pressure at a left-end boundary is given as

$$P^* = \left[(u^* - \bar{U}_R)\frac{(\gamma-1)}{2\gamma^{1/2}}\left(\frac{\rho_R}{P_R^{1/\gamma}}\right)^{1/2}\right]^{2\gamma/(\gamma-1)} \tag{27}$$

Piston Dynamics

The piston is assumed to have fixed mass, length, and frontal area. The piston state is given by a flag indicating whether the piston is constrained, its centroid position x_p and its velocity V_p. The governing differential equations are

$$\frac{'\mathrm{d}}{'\mathrm{d}t}x_p = V_p$$

$$\frac{'\mathrm{d}}{'\mathrm{d}t}V_p = \frac{1}{m_p}\left[A_p(P_B - P_F) + F_f\right] \tag{28}$$

where P_B and P_F are the pressures on the back and front piston faces, respectively, and F_f is the total frictional force. The frictional force is assumed to be due to the seal near the front face of the piston. The maximum magnitude of the frictional force is

$$|F_f|_{\max} = \mu_f A_{\text{seal}} P_F \tag{29}$$

where μ_f is the coefficient of friction of the seal material on the tube wall (taken to be 0.2), and A_{seal} is the effective frontal-area of the seal.

Diaphragms

Each diaphragm model is implemented as a flag for the status of the diaphragm (intact or burst) and a burst pressure. The effect of the diaphragm is coded directly into the simulation as a change in boundary conditions selected by the diaphragm's status flag. For example, two gas slugs initially separated by a diaphragm will have reflective boundary conditions applied at the diaphragm station. On rupture of the diaphragm, the applied boundary conditions will be changed to a data exchange condition.

Time Stepping

The state quantities for the piston and gas slugs are advanced from time level n to time level $n + 1$ with the predictor-corrector scheme

$$\begin{aligned}\Delta U^{(1)} &= \Delta t\frac{'\mathrm{d}U^{(n)}}{'\mathrm{d}t}\\ U^{(1)} &= U^{(n)} + \Delta U^{(1)}\\ \Delta U^{(2)} &= \Delta t\frac{'\mathrm{d}U^{(1)}}{'\mathrm{d}t}\\ U^{(n+1)} &= U^{(1)} + 1/2\left[\Delta U^{(2)} - \Delta U^{(1)}\right]\end{aligned} \tag{30}$$

where the superscripts 1 and 2 indicate intermediate results, and $\mathrm{d}U/\mathrm{d}t$ includes the rate of change of interface positions, cell momentum, cell energy, piston velocity, and piston position.

To maintain stability, the time step is restricted to

$$\Delta t \le \Delta t_{\text{allowed}} = \text{CFL}\,\Delta t_{\text{signal}} \tag{31}$$

where $\Delta t_{\text{allowed}}$ is the smallest value for all cells (and all gas slugs), and CFL is the specified Courant-Friedrichs-Lewy number. It is normally restricted to CFL = 0.25 in the simulations discussed later. For each cell, the inviscid signal time is approximated as

$$\Delta t_{\text{signal}} = \frac{\Delta x}{a} \tag{32}$$

Program Validation

The computer program was checked by running simulations for several simple gasdynamic systems. Simulations of the interaction of a shock wave with an abrupt area change[22] indicated that the quasi-one-dimensional formulation used here could reliably capture shocks and the effect of area changes. The coupling between the piston dynamics and gasdynamics was verified by considering the acceleration of a piston by an effectively infinite reservoir[23] and the impact of a shock wave with a light piston.[24] Viscous effects were checked by simulating the flow in a low-pressure shock tube.[25] Although the correct shock speed was computed for the low-pressure shock tube, the speed of the contact surface was not well approximated. This is because the modeling of the boundary layer, as discussed in the previous section, does not include mass transfer from the core flow into the boundary layer.[25,26] For estimating the performance of the T4 shock tunnel in terms of nozzle-supply pressure and enthalpy, this deficiency was considered to be minor.

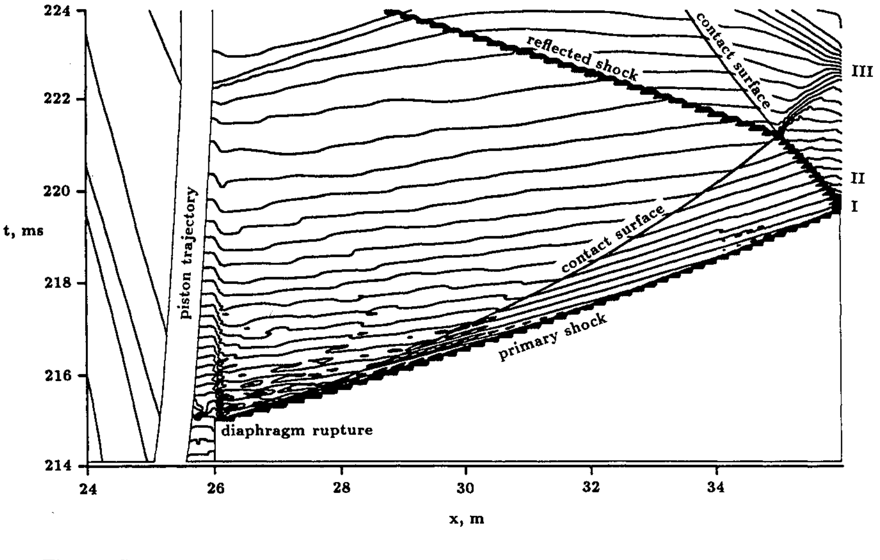

Fig. 4 Space-time diagram for shot 1098; contours are equally spaced values of log P.

Simulation Results

Three particular test cases were selected from the available tunnel data, and the key parameters are given in Table 2. Because the manifold between the compressed-air reservoir and the compression tube is pressurized just before piston release, the reservoir pressures given in Table 2 are 87.5% of the actual reservoir fill pressures. Initial gas temperatures were set to 296 K. Shot 1098 had a very low enthalpy of approximately 3 MJ/kg but was selected because absolute pressure measurements were made at a point 4 m downstream of the primary diaphragm and in the nozzle-supply (shock-reflection) region of the shock tube. The tunnel is not normally operated at such low enthalpies with a 100% helium driver. Shot 2499 was representative of a moderate enthalpy condition (15 MJ/kg) with reasonably high nozzle-supply pressure and a pure helium driver. Shot 1820 had a similar enthalpy to shot 2499 and was selected to demonstrate the increase of steady test time available when using a helium-argon mixture for the driver gas.[27] Each of these operating conditions had a nominal compression ratio of $\lambda = 60$.

The simulations were performed at several resolutions with the highest resolution calculations having 200 cells in the compressed-air gas slug, 400 cells in the driver gas slug, 400 cells in the test gas slug, and 25 cells in the nozzle/test section gas slug. Pressure estimates using half of these numbers of cells were typically within 5% of the results presented here.

Shot 1098

Figure 3 shows experimentally measured and computed pressure histories at two points in the shock tube. The first point (shock-speed measuring station 1, $x = 30.0$ m) is 4 m downstream of the primary diaphragm, whereas the second is located at $x = 35.95$ m in the shock reflection (or nozzle-supply region), a few centimeters upstream of the nozzle throat. For the simulation, time $t = 0$ corresponds to the release of the piston whereas, for the experiment, $t = 0$ is an arbitrary point a few milliseconds before shock reflection. The histories at shock station 1 (Figs. 3a and 3b) show reasonable quantitative agreement between simulation and experiment. The magnitude of pressure is well estimated for the primary shock, but the decay rate shortly after its passage ($t \simeq 217$ ms) is not so well approximated. Also, the estimated arrival time of the reflected shock is $t \simeq 6.93$ ms after the primary shock, which is a little longer than $\Delta t \simeq 6.43$ ms seen in the experiment.

The agreement between the experiment and simulation for the nozzle-supply pressure is good (Figs. 3c and 3d). The simulation provides good estimates for the pressure following the incident shock and the reflected shock (event I) and also captures the subsequent decay accurately (event II). The simulation shows a relatively long period between the incident shock and the reflected shock because of the gradual area variation used in the modeling. This gradual area variation, as opposed to the nearly planar endwall of the actual facility, delays the formation and propagation of the reflected shock. The simulation does not appear to be affected otherwise. Approximately 2.5 ms after shock reflection, the simulation shows a second decay in pressure (event III) due to the arrival of a reflected expansion (undertailoring). The experimental trace shows no sudden transition but decays by the same amount over a 2-ms period. This more gradual decay is attributed to the contact surface being somewhat diffuse in the experiment.

Figure 4 shows contours of the logarithm of pressure in (x, t) space. This diagram can be used to identify some of the key gasdynamic features and their interactions. Note the curvature of the trajectories of both the primary shock and the contact surface. The decay in contact surface speed is enhanced by the lack of mass transfer into the boundary layer. Also, because this particular condition is undertailored, the contact surface propagates back up the shock tube after interacting with the reflected shock. The expansion from this interaction can be seen arriving at the nozzle-supply region at $t \simeq 222.5$ ms (event III).

Table 2 Facility operating conditions

T4 shot number	Driver gas	Driver pressure, kPa	Test gas pressure, kPa	Reservoir pressure, MPa	Diaphragm rupture pressure, MPa
1098	Helium	61.6	450	4.90	57.0
1820	Helium-argon	61.6	35.0	4.90	57.0
2499	Helium	77.0	60.0	6.21	71.2

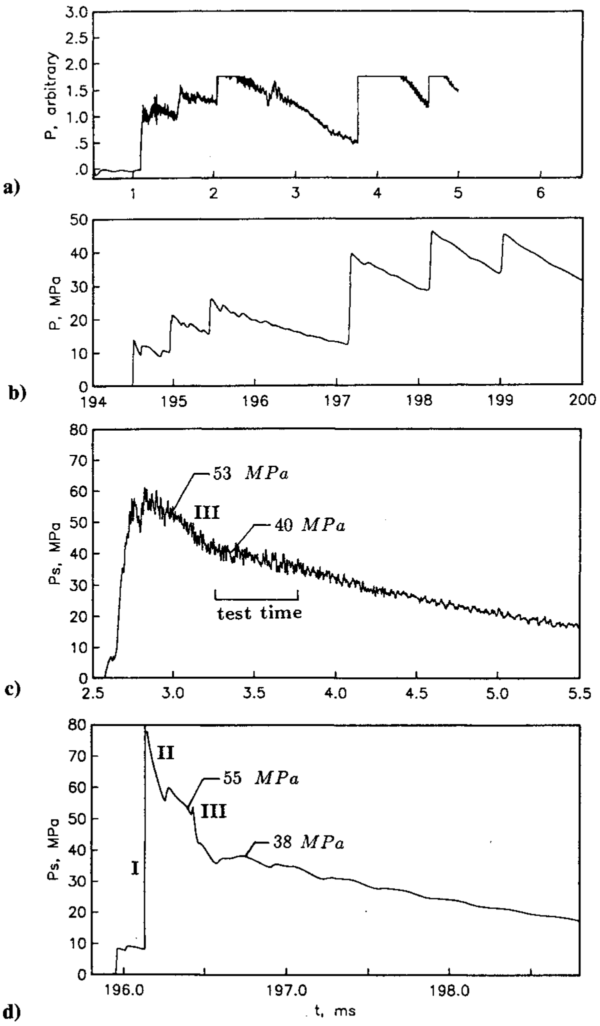

Fig. 5 Pressure histories for shot 2499: a) measured (combined) pressure at shock stations 1, 2, and 3; b) computed pressure at shock stations 1, 2, and 3; c) measured pressure in the nozzle-supply region; and d) computed pressure in the nozzle-supply region.

Shot 2499

For this shot, the pressure histories shown in Figs. 5a and 5b are a little difficult to interpret. The experimental trace was obtained by electrically joining the pressure transducers at shock stations 1, 2, and 3. The trace is a combination of the pressure histories at these locations and can only be used to obtain timing data. The simulation trace (Fig. 5b) was obtained by adding the pressure histories at each of the stations. Comparison of the timing events is again good for the incident shock but degrades somewhat for the reflected shock, especially at later times. This is not seen as a major defect of the code since most of the interesting gasdynamic processes (with respect to facility performance) are over shortly after shock reflection. Table 3 shows the incident shock speeds estimated for the simulation and the experiment. The shock speeds at $x = 31$, 33, and 35 m are average speeds based on the arrival times at shock stations 1, 2, and 3 and the nozzle-supply region. The initial simulation shock speed appears high but is within 4% of the ideal value. It then decreases rapidly and agrees closely with two out of three of the experimental results. The disagreement may be caused by different arrival times for the waves propagating from the driver. These waves are discussed later.

The simulation of nozzle-supply pressure is fairly good (refer to Figs. 5c and 5d) although there are a couple of distinct features in the computed pressure trace that are not seen in the experimental trace. Again, the decay in pressure due to undertailoring (event III) can be seen clearly in the simulation but not as clearly in the experimental trace. The pressure values before and after this event agree well. Refer to the figure for actual values.

A second obvious feature in the simulation trace is the large spike in pressure at shock reflection (event II). The experimental trace shows no such spike. Further information can be obtained from the (x, t) diagram (Fig. 6). The shock speed over the last 2 m of the shock tube is fairly constant at 3754 m/s ($M_s \simeq 10.9$). Assuming a quasisteady flow of air in chemical equilibrium, a post-incident shock pressure of 8.9 MPa and a shock-reflection pressure of 93.7 MPa can be estimated.[28] These values indicate that shock-reflection pressures should be quite high and that, in having a peak pressure of approximately 80 MPa, the simulation is self-consistent.

Prior to rupture of the primary diaphragm, the compression waves have coalesced into a weak shock ($M \simeq 1.02$) that bounces between the piston and the endwall of the compression tube (Fig. 6). It is one of these bounces that triggers the simulated rupture of the diaphragm. This diagram also shows the source of the oscillations on the pressure trace at shock stations 1, 2, and 3 (Fig. 5). These oscillations are due to a wave, initiated at primary diaphragm rupture, bouncing between the piston and the endwall of the compression tube. With each reflection from the endwall of the compression tube, there is a partial transmission into (and propagation along) the shock tube. One of these waves transmitted into the shock tube arrives shortly after shock reflection (event II) and causes a sudden decrease in nozzle-supply pressure (down to the levels seen in the experimental trace). Thus, it is postulated that these waves are part of the reason that actual shock tunnels provide lower nozzle-supply pressure than quasisteady analysis would estimate.

In an attempt to separate the viscous losses in the shock tube from the effects of the waves from the driver, the simulation was restarted just before diaphragm rupture and run without viscous losses. The pressure history in the nozzle-supply region for this inviscid simulation was similar in form to that for the viscous simulation but had pressures of 78 and 60 MPa before and after event III, respectively. The value of 78 MPa is significantly larger than the viscous result (55 MPa) but is still well below the ideal shock-reflection pressure of 206 MPa.

The computed histories of enthalpy and temperature in the nozzle-supply region are shown in Fig. 7. As expected, the relative fluctuations in enthalpy (and temperature) are significantly smaller than the pressure fluctuations. Also, the peak value of enthalpy is consistent with the quasisteady estimate of 15.4 MJ/kg.

The (x, t) diagram also gives some information on the piston dynamics. Noting the piston position at the time of primary dia-

Table 3 Shock speeds for shot 2499

x, m	Simulation, km/s	Experiment, km/s
26	5.45	——
31	4.35	4.36
33	4.08	4.03
35	4.00	3.79
36	3.75	——

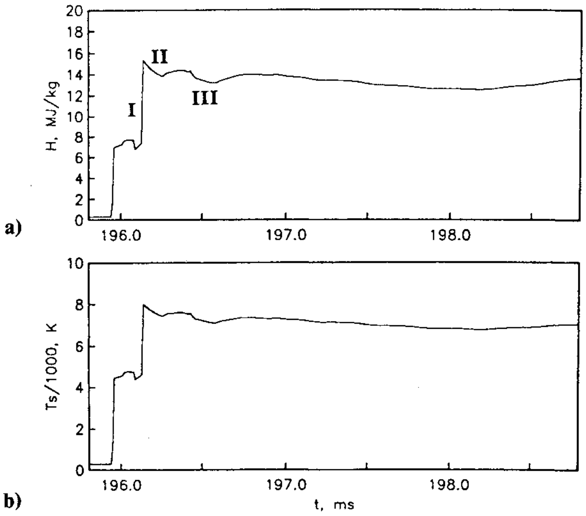

Fig. 7 Enthalpy and temperature histories in the nozzle-supply region for shot 2499: a) enthalpy and b) temperature.

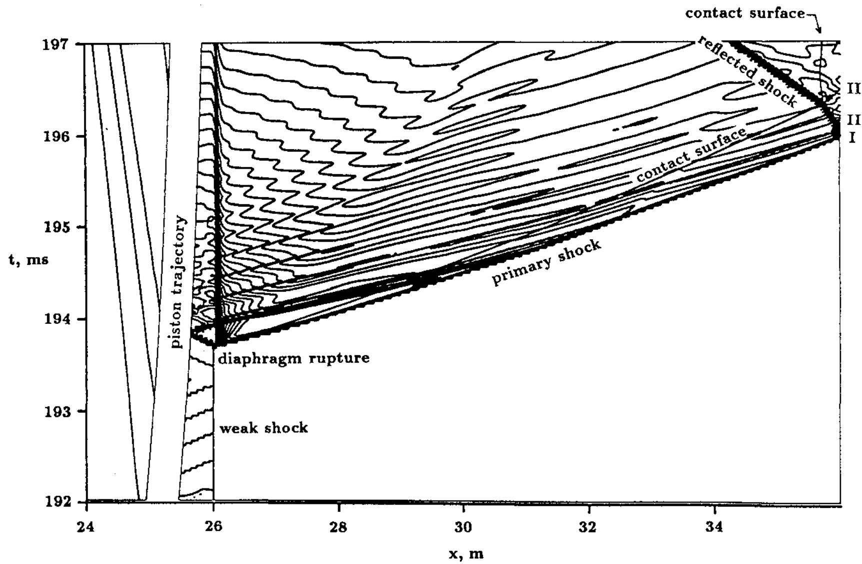

Fig. 6 Space-time diagram for shot 2499; contours are equally spaced values of log P.

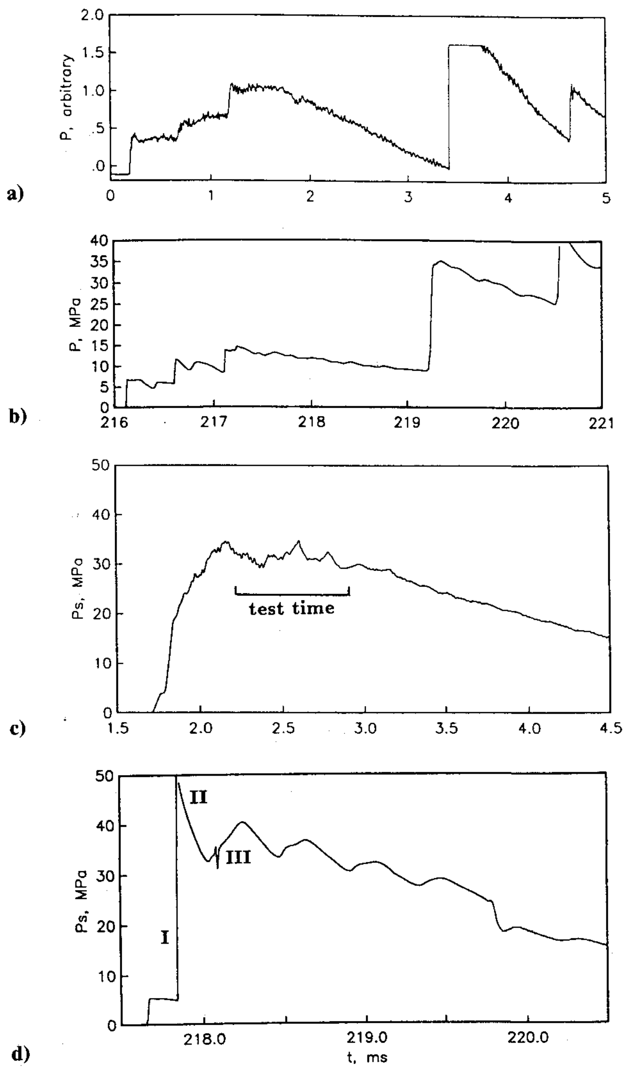

Fig. 8 Pressure histories for shot 1820: a) measured (combined) pressure at shock stations 1, 2, and 3; b) computed (combined) pressure; c) measured pressure in the nozzle-supply region; and d) computed pressure in the nozzle-supply region.

phragm rupture ($t = 0.1937$ s), one sees that the length of the driver gas slug is 0.365 m, which corresponds to an actual compression ratio of 70. This is slightly higher than the nominal value of 60 because of energy losses during the latter part of the compression process. At rupture, the speed of sound in the driver gas varies linearly from 3305 m/s at the front face of the piston to 3915 m/s near the diaphragm station. The temperature varies from 3155 to 4427 K. This can be compared with the ideal (isentropic) value of 4543 K for $\lambda = 60$.

During the compression process, the maximum piston speed was 182.2 m/s at $t = 0.1657$ s and $x_p = 20.67$ m. At this instant, the energies of the helium driver gas and the piston are 0.291 and 1.527 MJ, respectively. Approximately 10 μs before rupture, the piston has moved to $x_p = 25.40$ m and has a velocity of 89.6 m/s. At this point, the energy of the driver gas has increased to 1.495 MJ, whereas the kinetic energy of the piston has decreased to 0.369 MJ. Over the last 4.73 m of the compression stroke, the pusher gas near the piston has a (roughly) constant pressure of 1.165 MPa and does 0.227-MJ work on the piston. Given the 1.204 MJ energy increase in the driver gas, there has been a loss of 0.181 MJ or 13% of the total energy exchange during this part of the stroke.

Shot 1820

Taking conditions similar to shot 2499 and using a driver gas that is 10% argon by volume (and 90% helium) results in a nozzle-supply pressure that is much steadier over the millisecond test period (compare Fig. 8c with Fig. 5c). This operating condition is almost tailored. With a fairly constant supply pressure, secondary effects can be identified. Note the shallow dip in pressure shortly after shock reflection. This feature appears consistently for these conditions and for the equivalent conditions with 5-mm diaphragms[29] and is similar to the dip observed but not explained by Eitelberg et al.[2] In the simulation, these dips are exaggerated and persist for a larger time. Referring to the (x, t) diagram (Fig. 9), the dips in nozzle-supply pressure are seen to be coincident with the arrival of waves from the driver.

Other features in the simulated pressure history that need some explanation are the following:

1) The computed pressure levels that are approximately 10% higher than the experimentally measured levels.

2) The spike at shock reflection (event II): This has the same cause as the spike seen in the simulation of shot 2499.

3) The small glitch near the minimum of the first dip (event III): This glitch is the arrival of the signal from the reflected-shock/

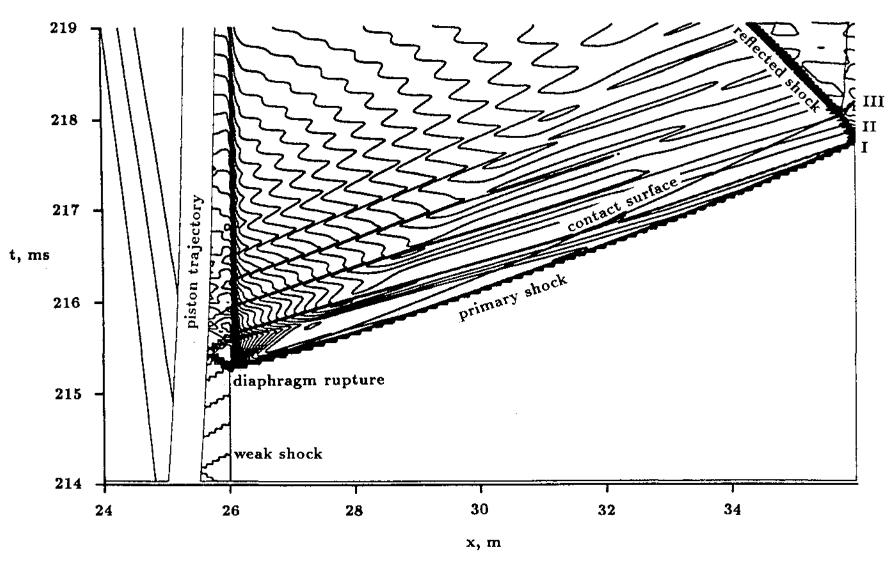

Fig. 9 Space-time diagram for shot 1820; contours are equally spaced values of log *P*.

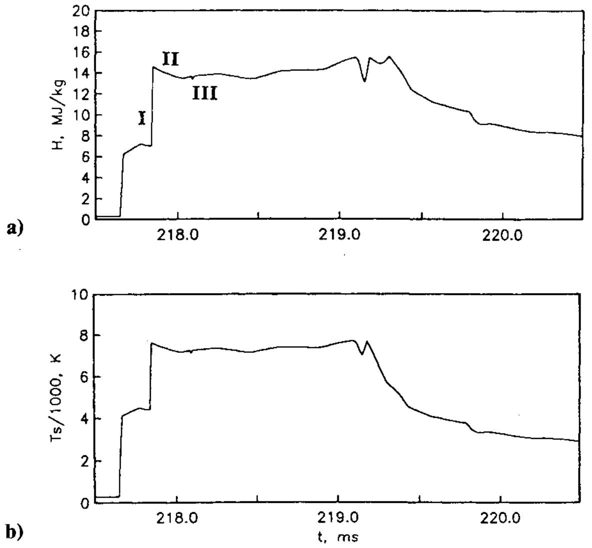

Fig. 10 Enthalpy and temperature histories in the nozzle-supply region for shot 1820: a) enthalpy and b) temperature.

contact-surface interaction. There is a small numerical artifact at the contact surface (which is a remnant of an error generated with the rupture of the primary diaphragm), and this pressure disturbance (at event III) is an echo from that artifact.

4) The sudden nozzle-supply pressure drop at $t = 219.8$ ms: This is caused by a lack of resolution when the driver gas cells reach the nozzle throat. Increasing the resolution delays this drop but does not affect the pressures estimated at earlier times.

The sensitivity of the nozzle-supply pressure to the fraction of argon in the driver gas was checked by running an equivalent simulation with a 15% argon mixture. The increase in argon fraction resulted in very little change in the average level of P_s during the test time but did result in a slightly lower rate of decay. Also, the period of the oscillation was slightly increased.

To complete the discussion, computed histories of enthalpy and temperature in the nozzle-supply region are shown in Fig. 10. As for shot 2499, the fluctuations in enthalpy are significantly smaller than the estimated fluctuations in pressure.

Concluding Remarks

The results presented here show that quasi-one-dimensional modeling of free-piston shock tunnels is an effective way to obtain facility performance data. Although this paper has focused on the T4 reflected-shock tunnel, the modeling is generic and may be applied to other facilities.

Of course, improvements can be made to the basic scheme. In particular, the present Lagrangian scheme has no mechanism for mass transfer through the boundary layer or by turbulent mixing at the contact surface. Addressing this problem would allow better estimates of the contact surface trajectory, the amount of uncontaminated test gas available after shock reflection, and the pressure history for undertailored (or overtailored) operating conditions. Also, the modeling of a sudden contraction by a gradual change in area can lead to problems, especially in the situation where the piston approaches close to the end of the compression tube. Lastly, the efficiency of the simulations could be greatly enhanced by making the discretization solution adaptive.

Acknowledgments

This work was sponsored by WBM-Stalker Pty. Ltd., Brisbane, Australia. The author is grateful for useful discussions with R. G. Morgan, R. Bakos, and R. J. Stalker of the University of Queensland and C. M. Gourlay and D. M. Jenkins of WBM. The author also wishes to thank the referees for their comments.

References

[1]Hornung, H. G., "Performance Data of the New Free-Piston Shock Tunnel at GALCIT," AIAA Paper 92-3943, July 1992.

[2]Eitelberg, G., McIntyre, T. J., Beck, W. H., and Lacey, J., "The High Enthalpy Shock Tunnel in Gottingen," AIAA Paper 92-3942, July 1992.

[3]Tamagno, J., Bakos, R., Pulsonetti, M., and Erdos, J., "Hypervelocity Real Gas Capabilities of GASL's Expansion Tube (HYPULSE) Facility," AIAA Paper 90-1390, June 1990.

[4]Deiwert, G. S., Strawa, A. W., Sharma, S. P., and Park, C., "Experimental Program for Real Gas Flow Code Validation at NASA Ames Research Center," *AGARD Symposium on Validation of Computational Fluid Mechanics*, Lisbon, Portugal, May 1988, pp. 21.1–21.15.

[5]Hornung, H. G., and Belanger, J., "Role and Techniques of Ground Testing for Simulation of Flows up to Orbital Speed," AIAA Paper 90-1377, June 1990.

[6] Groth, C. P. T., Gottlieb, J. J., and Sullivan, P. A., "Numerical Investigation of High-Temperature Effects in the UTIAS-RPI Hypersonic Impulse Tunnel," *Canadian Journal of Physics*, Vol. 69, No. 7, 1991, pp. 897–918.

[7]Burtschell, Y., Colas, P., Gubernatis, P., Zeitoun, D., Imbert, M., Houas, L., and Brun, R., "Numerical Simulation of A Free Piston Shock Tunnel," *17th International Symposium on Shock Waves and Shock Tubes*, Lehigh, PA, 1989, pp. 576–581.

[8]Maus, J., Laster, M., and Hornung, H., "The G-Range Impulse Facility—A High-Performance Free-Piston Shock Tunnel," AIAA Paper 92-3946, July 1992.

[9]Cambier, J. L., Tokarcik, S., and Prabhu, D. K., "Numerical Simulations of Unsteady Flow In A Hypersonic Shock Tunnel Facility," AIAA Paper 92-4029, July 1992.

[10]Stalker, R. J., and Morgan, R. G., "The University of Queensland Free Piston Shock Tunnel T4—Initial Operation and Preliminary Calibration," *Fourth National Space Symposium*, Adelaide, Australia, 1988.

[11]Von Neumann, J., and Richtmyer, R. D., "A Method for the Numerical Calculation of Hydrodynamic Shocks," *Journal of Applied Physics*, Vol. 21, March 1950, pp. 232–237.

[12]Srinivasan, S., Tannehill, J. C., and Weilmuenster, K. J., "Simplified Curve Fits for the Thermodynamic Properties of Equilibrium Air," NASA Reference Publication 1181, Aug. 1987.

[13]Schlichting, H., *Boundary-Layer Theory*, McGraw-Hill, New York, 1968, Chap. 20.

[14]Holman, J. P., *Heat Transfer*, McGraw Hill, New York, 1981.

[15]Liepmann, H. W., and Goddard, F. E., "Note on the Mach Number Effect upon the Skin Friction of Rough Surfaces," *Journal of the Aeronautical Sciences*, Vol. 24, No. 10, 1957, p. 781.

[16]Wilke, C. R., "A Viscosity Equation for Gas Mixtures," *Journal of Chemical Physics*, Vol. 18, 1950, pp. 517–519.

[17]Jacobs, P. A., "An Approximate Riemann Solver for Hypervelocity Flows," *AIAA Journal*, Vol. 30, No. 10, 1992, pp. 2558–2561.

[18]Ben-Artzi, M., "The Generalized Riemann Problem for Reactive Flows," *Journal of Computational Physics*, Vol. 81, No. 1, 1989, pp. 70–101.

[19]Ben-Artzi, M., and Falcovitz, J., "An Upwind Second-Order Scheme for Compressible Duct Flows," *SIAM Journal on Scientific and Statistical Computing*, Vol. 7, No. 3, 1986, pp. 744–768.

[20]Lappas, A., Leonard, T., and Dimotakis, P. E., "An Adaptive Lagrangian Method for Computing 1D Reacting and Non-Reacting Flows," *Journal of Computational Physics*, Vol. 104, No. 2, 1993, pp. 361–376.

[21]Sweby, P. K., "High Resolution Schemes Using Flux Limiters for Hyperbolic Conservation Laws," *SIAM Journal of Numerical Analysis*, Vol. 21, 1984, pp. 995–1010.

[22]Salas, M. D., "Shock Wave Interaction with an Abrupt Area Change," NASA TP 3113, 1991.

[23]Berggren, R. E., and Reynolds, R. M., "The Light-Gas-Gun Model Launcher," *Ballistic Range Technology*, AGARDograph 138, 1970, pp. 11–94.

[24]Meyer, R. F., "The Impact of a Shock Wave on a Moveable Wall," *Journal of Fluid Mechanics*, Vol. 3, 1957, pp. 309–323.

[25]Duff, R. E., "Shock-Tube Performance at Low Initial Pressure," *Physics of Fluids*, Vol. 2, No. 2, 1959, pp. 207–216.

[26]Mirels, H., "Test Time in Low-Pressure Shock Tubes," *The Physics of Fluids*, Vol. 6, No. 9, 1963, pp. 1201–1214.

[27]Jenkins, D. M., Stalker, R. J., and Morrison, W. R. B., "Performance Considerations in the Operation of Free-Piston Driven Hypersonic Test Facilities," *18th International Symposium on Shock Waves* (Sendai, Japan), 1991.

[28]McIntosh, M. K., "Computer Program for the Numerical Calculation of Frozen and Equilibrium Conditions in Shock Tunnels," Technical Rept., Australian National Univ., 1968.

[29]Bakos, R., private communication, Dept. of Mechanical Engineering, Univ. of Queensland, St. Lucia, Queensland, Australia, 1992.